Alloy Design for Additive Manufacturing: Early-Stage Oxidation of Nickel-Based Superalloys

JOSEPH N. GHOUSSOUB, SATOSHI UTADA, FERNANDO PEDRAZA, WILLIAM J.B. DICK-CLELAND, YUANBO T. TANG, and ROGER C. REED

This body of work aims to inform alloy design for additive manufacturing by investigating the early-stage oxidation behavior of Ni-based superalloys processed by laser-powder bed fusion. The oxidation of 14 Ni-based superalloys—some novel and some heritage—at 1000 °C for 24 hours is studied through thermo-gravimetric analysis. The mass gain, oxide layer thickness, oxide scale composition, and γ' depletion zone size are measured. The influence of the alloy composition on these variables is assessed in order to elucidate how increasingly processable and oxidation resistant alloys can be developed. The alloy compositions with Al content greater than 9 at. pct form continuous Al_2O_3 scales at 1000 °C and display markedly lower parabolic rate constants, mass gain, oxide layer thickness, and γ' depletion zone size. The alloys of lesser Al content have reduced oxidation resistance and formed oxide scales of predominantly Cr_2O_3. Alloys with Ti content of 2.7 at. pct and greater formed Ti-rich oxide phases in their oxide scales as well as TiN subscale. A trade-off between alloy processability and oxidation resistance is identified, dictated by the deleterious effect of Al content on the ductility dip and the benefit of Al for oxidation resistance. A property space along the pareto front is highlighted which is ideal for having oxidation resistance and processability.

I. INTRODUCTION

METAL alloy processing by additive manufacturing (AM) offers many advantages such as accelerated rapid prototyping and increased geometric design capabilities.[1] In recent years, the development of alloys tailored specifically for 3D printing has began taking place as AM technologies have matured.[2–4] Thus far, the targeted properties of these novel alloys have been primarily tensile strength, creep life, and of course their manufacturability/processability—defined as their resistance to processing induced defects such as cracks. However, there are currently limited examples of alloy design for AM which emphasize the resistance of alloys to oxidation and environmental degradation.[5] The need to design for oxidation resistance stems from the deleterious impact of high-temperature oxidation and its associated damage mechanisms such as oxidation-assisted cracking,[6] dwell fatigue crack growth,[7] and their interactions.[8] In light of these degradation mechanisms, the design of AM alloys with a focus on oxidation resistance cannot be disregarded. Here, we aim to address the lack of alloy design for AM and oxidation resistance by studying the behavior of a range of alloy compositions and elucidating how oxidation performance trades off against other key alloy design metrics.

What methodologies can be applied to gain insights into developing AM alloys with increased oxidation resistance? Examples of previously employed strategies for investigating alloys produced by conventional methods include thermodynamic and kinetic modeling[9] as well as systematic experimental trials.[10–12] Motivated by the absence of significant pre-existing data on the oxidation performance of AM produced superalloys, we choose to apply the experimental route here.

Can analysis of more readily available conventionally processed alloys be used to develop oxidation resistant superalloys for AM? The differences highlighted between the oxidation behavior of additively manufactured and conventionally processed material suggests otherwise. Pistor *et al.* highlight that differences in

JOSEPH N. GHOUSSOUB, SATOSHI UTADA, and YUANBO T. TANG are with the Department of Materials, University of Oxford, Parks Road, Oxford, OX1 3PH, UK. Contact e-mail: joseph.ghoussoub@materials.ox.ac.uk FERNANDO PEDRAZA is with the Laboratoire des Sciences de l' Ingénieur pour l' Environnement, La Rochelle Université, Avenue Michel Crépeau, 17042 La Rochelle Cedex 1, France. WILLIAM J B DICKCLELAND is with the Alloyed Ltd. Yarnton, Kidlington OX5 1QU, UK. ROGER C. REED is with the Department of Materials, University of Oxford and also with the Department of Engineering Science, University of Oxford, Parks Road, Oxford, OX1 3PJ, UK.
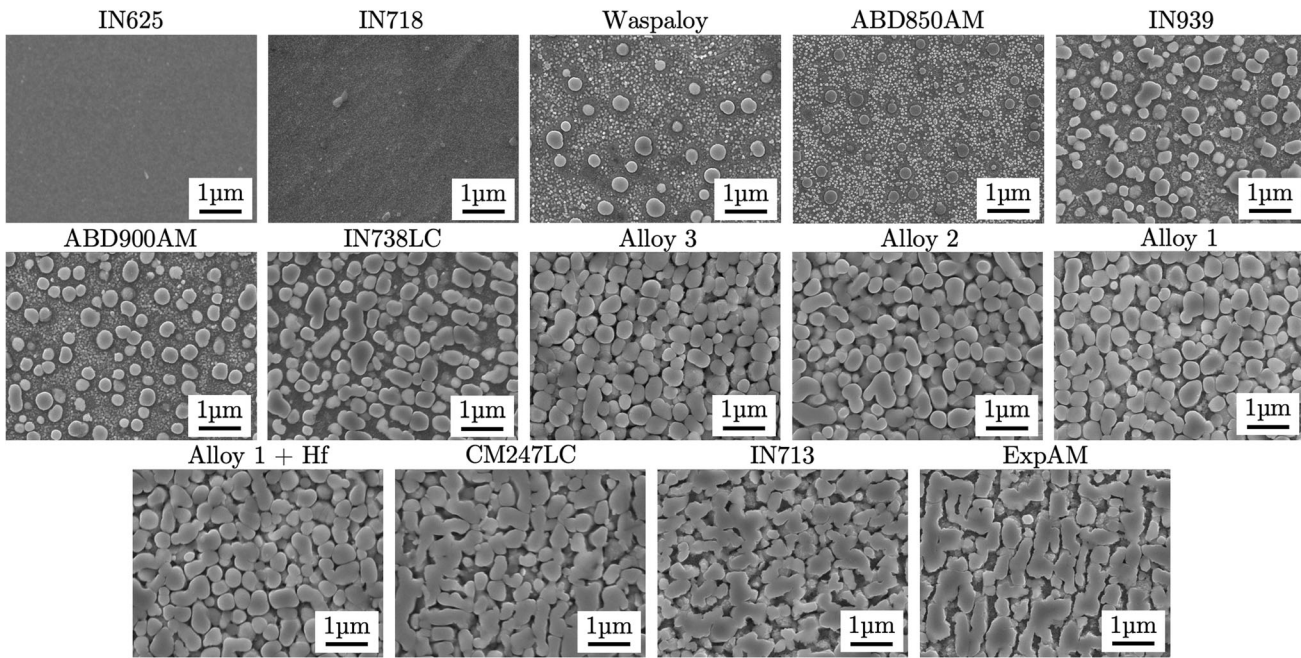
Fig. 1—SEM micrographs showing the precipitation of γ' in the bulk of each alloy after 24 h at 1000 °C. It is noted that since IN625 and IN718 do not precipitate any substantial γ', here, the contrast is very low.

segregation between AM samples and Brigdman samples cause substantial changes in oxide layer homogeneity driven by segregation.[13] Furthermore, Julliet *et al.* highlighted how for AM-processed IN718, cation diffusion is arrested whereas the opposite holds true for forged 718;[14] furthermore, it has been shown that small compositional and microstructural differences result in varying levels of degradation—in the form of oxide spallation—when comparing material processed by AM as opposed to conventionally processed,[15] Here, we study 14 different compositions processed in the same manner. These alloys cover a wide compositional space with widely varying equilibrium γ' volume fraction—illustrated in Figure 1. In what follows, we present a substantial experimental dataset describing the oxidation behavior of additively processed compositions which is interpreted to yield one of first studies towards alloy design for oxidation resistance of AM alloys.

II. EXPERIMENTAL METHODS

A. *Alloy Compositions and Feedstock Material*

A total of 14 different alloy compositions were analyzed. Their compositions—measured by Inductively coupled plasma-optical emission spectrometry (ICP-OES) and ICP-combustion analysis—are given in at. pct in Table I. The feedstock powders were produced by argon gas atomization (prepared by Aubert & Duval) with median particle diameter (D50) between 32.1 and 32.7 μm. Of the 14 compositions studied here, 7 are heritage grades (CM247LC, IN625, IN713, IN718, IN738LC, IN939, and Waspaloy), while the remaining 7 are novel compositions. ABD850AM and

ABD900AM are alloys designed for AM previously studied in Reference 16, Alloys 1 to 3 are experimental compositions designed for AM studied in Reference 5, Alloy 1 + Hf is an Hf containing variant of Alloy 1, and the remaining alloy is an experimental AM alloy we refer to here as "ExpAM." While the alloy compositions being analyzed do not make up a discrete design of experiments to reveal the nature of specific compositional interactions, they are sufficiently varied as to give insight into key overarching questions such as the critical thresholds of Al, Cr, and Ti content which change the nature of oxide scales formed at elevated temperatures. The sliding scale of these compositions is best illustrated by their varied equilibrium γ' volume fraction (after 24 hours at 1000 °C) shown in Figure 1. The γ' precipitate volume fraction is greater in the alloys with greater Al, Ti, Ta, and Nb content such as ExpAM and CM247LC in contrast to alloys of more moderate γ' content such as ABD850AM and Waspaloy. In order to test and characterize these compositions, additively manufactured cubes were produced by laser-powder bed fusion (L-PBF) at Alloyed Ltd. using a Renishaw AM 400 pulsed fiber laser system of wavelength 1075 nm under an argon atmosphere with a build plate size of $80 \times 80 \times 64$ mm^3. The processing parameters employed were: laser power 200 W, laser focal spot diameter 70 μm, powder layer thickness 30 μm, and pulse exposure time 60 μs. A 'meander' laser scan path pattern was used with hatch spacing of 70 μm and laser scan speed of 0.875 m/s, the path frame of reference was rotated by 67 deg with each layer added. In order to produce a high-quality surface finish, the laser traced the border of the sample after each layer, the laser speed on the borders was reduced to 0.5 m/s. Each alloy powder was processed with these parameters.

Table I. Measured Alloy Powder Compositions (At. Pct)

Alloy	Ni	Al	Co	Cr	Fe	Mo	Nb	Ta	Ti	W	C	B	Hf
ABD850AM	bal.	2.9	17.9	22.5	—	1.24	0.40	0.16	2.76	1.55	0.049	0.016	—
ABD900AM	bal.	4.5	20.0	19.1	—	1.27	1.16	0.39	2.90	0.97	0.228	0.016	—
Alloy 1	bal.	11.5	19.2	10.2	—	0.75	1.38	1.08	0.15	2.23	0.181	0.030	—
Alloy 1 + Hf	bal.	11.3	19.0	10.0	—	0.72	1.38	1.10	0.14	2.23	0.221	0.020	0.16
Alloy 2	bal.	10.4	19.4	10.3	—	0.75	1.82	1.50	0.15	2.27	0.185	0.028	—
Alloy 3	bal.	9.6	19.8	10.2	—	0.78	2.35	1.86	0.15	2.36	0.158	0.027	—
CM247LC	bal.	12.2	9.4	9.5	—	0.34	—	1.06	0.91	3.14	0.349	0.111	0.47
ExpAM	bal.	11.6	7.2	12.6	—	1.17	0.66	—	2.34	1.13	0.019	0.000	—
IN625	bal.	—	—	22.9	4.1	5.49	2.35	—	0.21	—	0.244	0.000	—
IN713	bal.	12.2	—	12.7	0.2	2.47	1.24	—	0.81	—	0.275	0.051	—
IN718	bal.	1.3	1.1	21.4	17.8	1.93	3.05	—	0.97	—	0.385	0.003	—
IN738LC	bal.	7.0	8.2	17.2	0.02	1.03	0.53	0.53	3.91	0.84	0.521	0.058	—
IN939	bal.	3.8	18.0	24.4	—	—	0.61	0.41	4.24	0.49	0.751	0.057	—
Waspaloy	bal.	2.7	11.6	21.9	0.04	2.59	—	0.00	3.56	—	0.237	0.042	—

B. Thermo-gravimetric Analysis

A NETZSCH STA 449 F1 Jupiter was used for thermo-gravimetric analysis (TGA) to assess the mass gain of each alloy under oxidizing conditions. Specimens of dimensions 10 mm × 10 mm × 1 mm were cut perpendicular to the build direction and polished to a mirror finish with 4000 grit SiC paper. Specimens were tested in the as-printed state, where they are initially devoid of γ'—given this apparatus and specific processing conditions.[17] The tests were carried out in 5 steps; a protective Ar gas flow is run for 1 hour to ensure equilibrium of the system. This was followed by an increase of temperature at a rate of 20 K/min to the test temperature of 1000 °C followed by another hold for 30 minutes under a protective Ar atmosphere and then the onset of the oxidizing laboratory air flow at 50 ml/min for 24 hours. After this period, the sample is cooled to room temperature at 20 K/min. The evolution of mass gain was analyzed starting at the onset of oxidizing air. In this study, testing was performed at a single temperature of 1000 °C and for 24 hours to be economical as well as to enable the high throughput testing of a wide range of alloys. Further testing at a range of temperatures and for longer time periods is reserved for future works. The use of 24 hours tests allowed for the assessment of the oxidation behavior and microstructure of the alloys in their early stages. The test temperature of 1000 °C is selected motivated by the objective of developing polycrystalline materials for increasingly elevated operating temperatures.

C. Microstructural Characterization

The spatial distribution of elements and chemical composition of phases in the oxide layers following testing was quantified with a Zeiss Merlin Gemini 2 field emission gun scanning electron microscope (FEG-SEM). This was equipped with an Oxford Instruments XMax 150mm/mm^2 energy-dispersive X-ray spectroscopy (EDX) detector. Maps were acquired with an accelerating voltage of 15 kV and probe current 500 pA. Oxford Instruments Aztec software was employed to perform phase mapping; the analyzed phase function was employed to generate phase maps and identify the nature of oxide scales. To acquire phase maps, the software generates an initial automated map based on groups of adjacent pixels with similar stoichiometric coefficients. This map was manually confirmed by cross referencing the phase boundaries with corresponding BSE images and observing the EDX spectra of the pixels at phase boundaries. The literature was cross referenced in order to give increased confidence in the nature of the phases detected, this is discussed in subsequent sections. This methodology enabled high throughput analysis of the oxide scales for relative comparison albeit at the cost of the increased certainty afforded by the more conventional x-ray diffraction (XRD) methodologies.

The γ' that precipitated in the bulk of the samples during testing was characterized by SEM following an electrolytic etching with 10 pct phosphoric acid at 3 V for 5 seconds. The oxide layers of each alloy were characterized by mounting the TGA samples in conductive resin followed by polishing, low force polishing was used to ensure high-quality edge retention. A set of 10 backscattered electron (BSE) images were taken of the oxide layer and depletion zone in each alloy to quantify their thickness using ImageJ. The layer thickness was measured manually, for each image, 30 line measurements were taken across the thickness of the continuous oxide scale region. The same was performed for the gamma prime depletion zone size. The boundary between the gamma prime depleted region and the gamma region was distinct and allowed for consistent measurement. Only the continuous scale region was considered in the thickness measurement. IN625 and IN718 were excluded from the γ' depletion zone size analysis as no γ' was observed.

III. RESULTS AND DISCUSSION

A. Mass Gain and Growth Kinetics

Figure 2 summarizes the results of thermo-gravimetric analysis. In all the alloys analyzed, an initial transient behavior was apparent in the first 1 to 6 hours. IN625 and IN718 demonstrated a second transient behavior
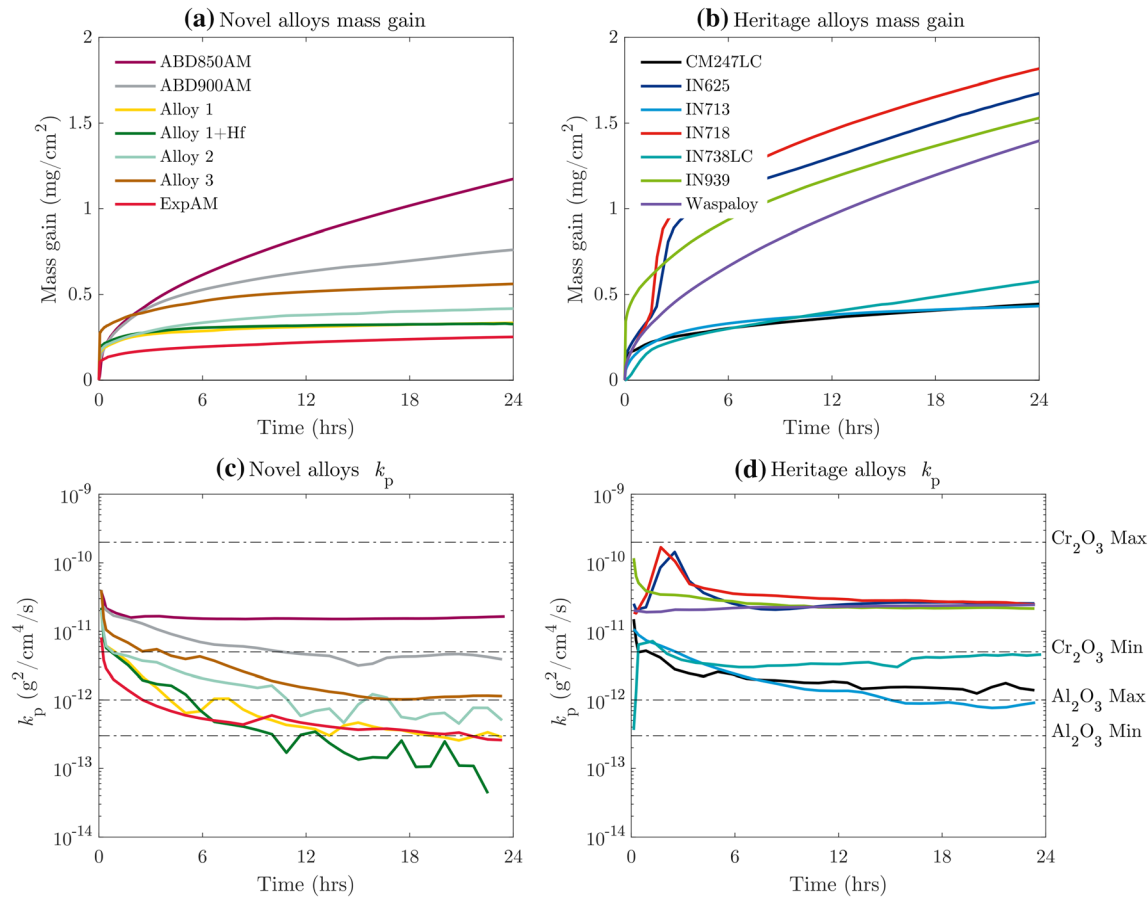
Fig. 2—Results of thermo-gravimetric analysis at 1000 °C for 24 h for (a) the novel alloys and (b) the heritage alloys and the parabolic rate constant k_p over the duration of the test for (c) the novel alloys and (d) the heritage alloys.

between 2 and 4 hours where the oxidation rate increased rather than decreased; in these regimes, thermodynamic equilibrium has not yet been reached. ExpAM exhibited the least mass gain under the test conditions employed here. ABD900AM and ABD850AM showed very similar mass gain for the first 4 hours after which ABD900AM tapered off and the rate of mass gain decreased comparatively. Of the heritage alloys, IN625 and IN718 gained the most mass in this time frame, and this was anticipated as they were not designed for use at 1000 °C. IN713 and CM247LC gained the least mass of the heritage alloys and did so at a similar rate, whereas IN738LC—which oxidized to a slightly larger degree—gained mass more slowly initially but surpassed them after ~10 hours. Further analysis of the impact of composition on mass gain is performed in subsequent sections. Figures 2(c) and (d) shows the parabolic rate constant determined for each composition. The parabolic rate constant k_p was measured by the standard method[18] as follows:

$$\left(\frac{\Delta m}{A}\right)^2 = k_p t, \qquad [1]$$

where Δm is the mass change, A is the surface area, and t is time. This analysis allows for an interrogation of the assumptions needed for the classic parabolic growth rate law: pure diffusion control and no transient regime. Estimates of the expected minimum and maximum values of the parabolic growth rate for Al_2O_3, and Cr_2O_3, found in the literature[19] are superimposed on Figures 2(c) and (d). Of the heritage alloys, IN625, IN718, IN939, and Waspaloy all fall well within the range of Cr_2O_3 growth, whereas CM247LC and IN713 appear to be in the Al_2O_3 growth regime. Of the novel alloys, only ABD850AM and ABD900AM grew oxides at Cr_2O_3-like rates. The remaining alloys trended towards the growth rates of Al_2O_3. The initial transient behavior observed in the mass gain curves of IN625 and IN718 manifests as an increasing slope of $k_p - t$ until direct oxidation ends.

B. Oxide Scale Formation and Sub-Scale Microstructure

Understanding the nature of the oxidation layers formed in each composition is key to mapping the composition, microstructure, and property relationships of these alloys. BSE micrographs shown in Figure 3 illustrate the variety of scales formed. The two alloys which underwent the greatest mass gain—IN625 and IN718—exhibited thicker oxide scales. IN625, IN718, Waspaloy, ABD850AM, and IN939 were the most prone to mass gain in the 24 hours test. The ABD900AM and IN738LC alloys underwent moderate
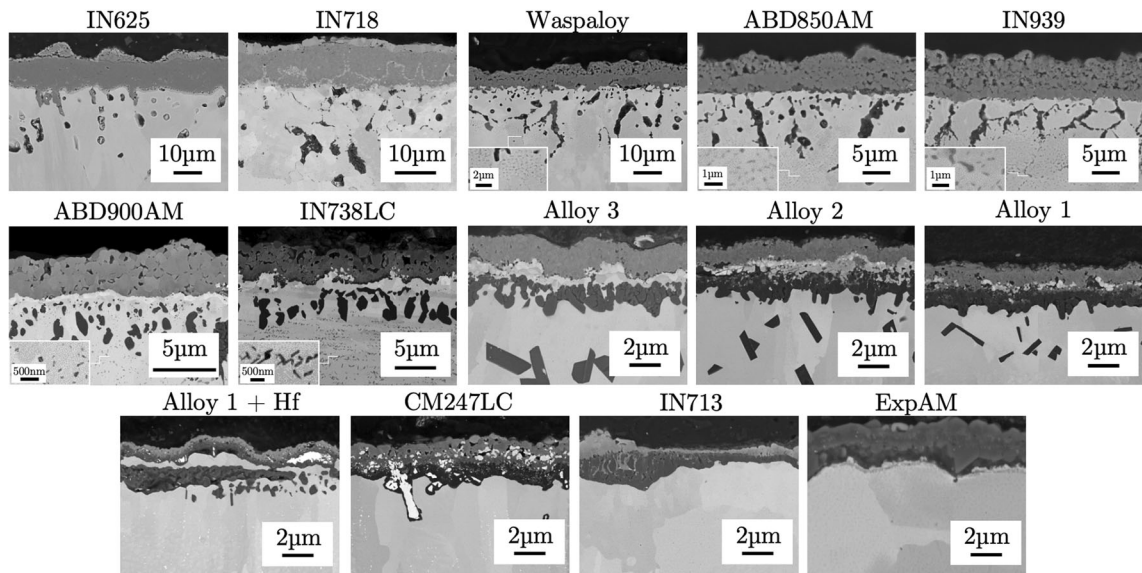
Fig. 3—BSE micrographs showing the oxide layers formed at the surface of each alloy after 24 h at 1000 °C.
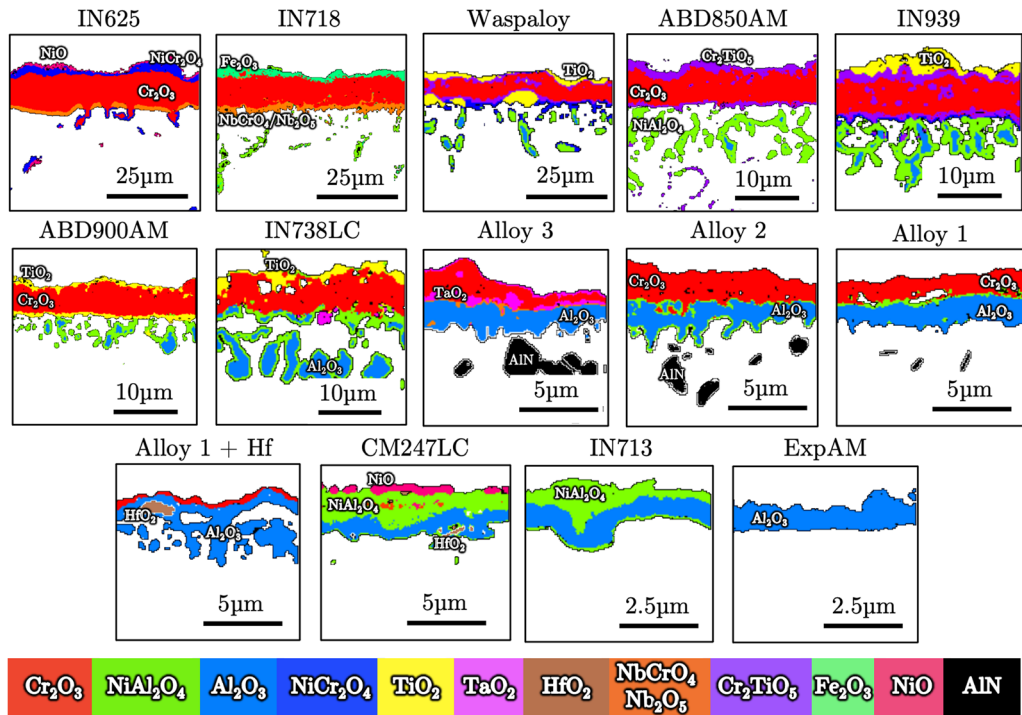

Fig. 4—Phases at the surface of each alloy identified by high-resolution SEM-EDX after 24 h at 1000 °C.

mass gain during testing—both had discontinuous Al_2O_3 dispersed below their oxide scales, indicating insufficient Al content and thermodynamic driving force for the formation of a stable Al_2O_3 layer. Blocky AlN is apparent below the oxide layers of Alloys 1, 2, 3, and Alloy 1 + Hf. Compositional analysis of their feedstock powders determined the N content to be < 0.005 wt pct; therefore, the N uptake and resulting presence of AlN is concluded to have occurred during testing. This is discussed further in subsequent sections. Very fine TiN

is visible in Waspaloy, ABD850AM, and IN939; a mixture of TiN and AlN precipitated in ABD900AM and IN738LC. The formation of these nitrides is well explained by Krupp et al.[20] and Han et al.[21] who highlight the inability of the Cr_2O_3 to prevent N transport and the need for discontinuities in an Al_2O_3 layer to permit N transport through. Hf is present in the oxide scales of CM247LC and Alloy 1 + Hf, appearing as a bright white phase in the BSE images—a result of Hf's elevated atomic number. The oxide scales were

homogeneous across the edges, and this is attributed to the controlled environment in the TGA and high degree of surface polish achieved prior to testing. The variability of the oxide layer thicknesses is quantified in subsequent sections.

The EDX map analysis of the oxide layers shown in Figure 4 reveals which oxides formed in each alloy. In IN625, an outer NiO oxide layer was detected followed by $NiCr_2O_4$, a thick Cr_2O_3 layer then what is presumed $NbCrO_4$ and/or Nb_2O_5. These findings are largely consistent with those of Vesel *et al.*[22] and Kumar *et al.*[23] who highlight IN625's tendency towards formation of Nb_2O_5 and $NiCr_2O_4$. IN718 formed an outer layer of Fe_2O_3, followed by Cr_2O_3 with Nb oxide below, $NiAl_2O_4$ was detected in discontinuous form subsurface. Waspaloy, ABD850AM, and IN939 formed similar oxide scales consisting a of Cr_2O_3 layer with Ti oxides on the inner and outer scales and Al-rich branches subscale. Waspaloy and IN939 formed discontinuous TiO_2 on the outmost layer with Cr_2TiO_5 below, the Cr_2O_3 and inter Cr_2TiO_5 layer a thin $NiCr_2O_4$ was observed. The Al-rich subsurface particles were Al_2O_3 with a $NiAl_2O_4$ transition layer. The phases in Waspaloy and IN939 detected here were in agreement with the findings of[24,25] which differed only in that they reported the presence of Ta and Nb oxides in IN939 which were not observed in the present study. IN738LC and ABD900AM both developed TiO_2 on their outer scale but no Cr_2TiO_5, each developed a continuous Cr_2O_3 layer though IN738LC's layer was highly porous. Large Al_2O_3 precipitated subscale in IN738LC with a transient layer of $NiAl_2O_4$; furthermore, TaO_2 particles were dispersed in the $Al_2O_3/NiAl_2O_4$ layer underneath the Cr_2O_3. Litz *et al.* reported similar findings but additionally reported the presence of NiO, NbO_2, and TiO_2.[25]

Alloys 1 to 3, and Alloy 1 + Hf each exhibited a Cr_2O_3 layer and a stable Al_2O_3 layer of approximately similar size beneath. For Alloys 1 and 2, an $NiAl_2O_4$ layer was found between the two main Cr and Al layers. Naturally Alloy 1 + Hf was the only alloy to have Hf oxides in its layer. Some porosity was observed in the oxide scales of these 5 alloys, though no trend in severity across compositions was observed.

CM247LC, IN713, and ExpAM did not form Cr_2O_3 layers. In ExpAM only, a stable Al_2O_3 layer was observed. CM247LC had a discontinuous NiO outermost layer followed by an $NiAl_2O_4$ layer with Nb, Ni, and Hf-oxide phases inside then a continuous Al_2O_3 inner layer. These findings are consistent with the literature though the tendency of CM247LC to form TiO_2 and Ta_2O_5 has also been highlighted in other works.[26,27] Al_2O_3 with $NiAl_2O_4$ on either side was observed in IN713, congruous with the findings of the literature.[28,29]

The magnitude of this depletion zone was highly alloy dependent. The observed γ' depletion zone was largest in Waspaloy followed by ABD850AM. The depletion zone size observed was considerably smaller in the alloys that formed continuous Al_2O_3 scales, this is illustrated in Figure 5. The alloys with greater Al content were able to readily form continuous oxide scales that in turn acted
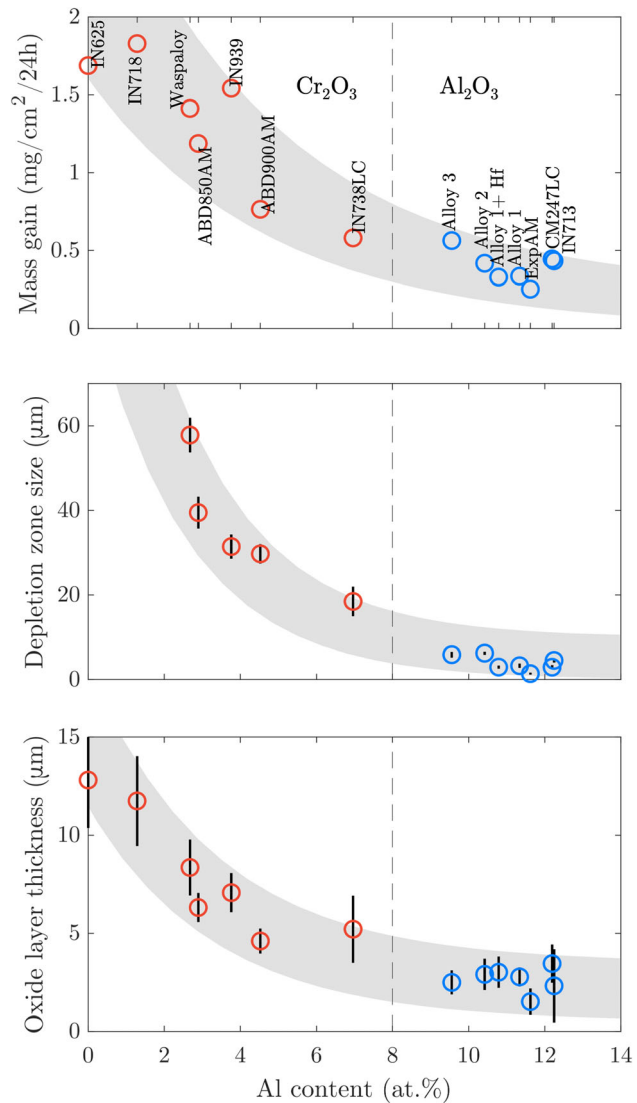

Fig. 5—Summary of the measured mass gain, γ' depletion zone size, and oxide layer thickness as a function of Al content (at. pct).

as a passivation layer limiting further depletion of the Al-rich γ'. In the IN625 and IN718 alloys—which did not precipitate γ' and did not form an Al_2O_3 oxide scale—no depletion zone was observed. Analysis of the oxide layer thickness shows IN625 and IN718 developed the thickest oxide layers. ExpAM and IN713 developed the smallest layers, but the scale of IN713 had a less uniform thickness as illustrated by the wide measured standard deviation. The oxide layer of IN713 in Figure 4 exemplifies how this variability manifests itself: a pocket of $NiAl_2O_4$ sitting atop Al_2O_3 that has depressed into the bulk of material. IN738LC was the only other alloy to have an observably more variable oxide layer thickness.

C. On the Influence of Composition on Oxide Scale Formation and Mass Gain

Figure 5 shows how increasing Al content results in a reduction of measured mass gain, depletion zone size,
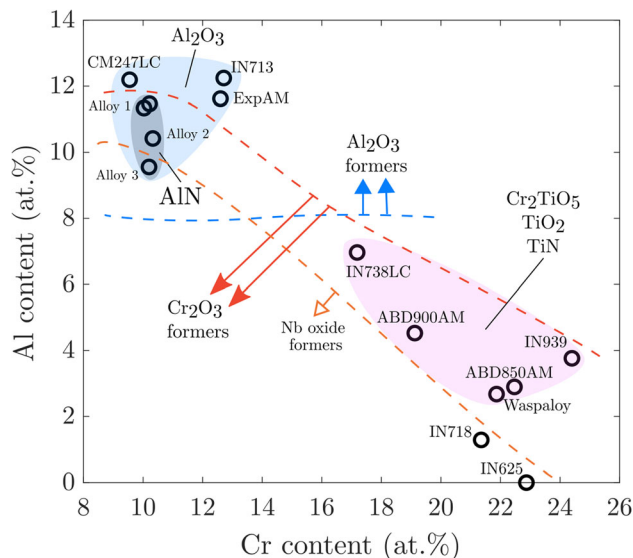
Fig. 6—Scatter plot of Al *vs* Cr content (at. pct) with highlighted compositional spaces where different oxides formed after 24 h at 1000 °C.

and oxide thickness. In particular, the 7 compositions with Al content greater than approximately 7 at. pct had greatly reduced oxidation kinetics—owing to the formation of continuous alumina scales.[30] None of the 7 alloys with Al content < 9 at. pct developed a continuous Al_2O_3 oxide layer; instead they formed Cr_2O_3 scales. The thickness of the oxide layers of the Cr_2O_3 forming alloys ranged between 4 and 14 μm. The alloys with greater oxide layer thickness had greater γ' depletion zone sizes; this was due to dissolution of γ' and subsequent diffusion of Ti to the TiO_2 and Cr_2TiO_5 oxide scales. The Al_2O_3 forming alloys had smaller depletion zones as the stable Al_2O_3 layers substantially reduced the oxidation rate. Mass gain and oxide layer thickness correlated well since the diffusion of elements in the bulk and their bonding with O^{2-} resulted in the growth of oxide at the surface. The depletion zone sizes and oxide layer thicknesses of most of the Al_2O_3 forming alloys were not statistically distinguishable; the exception was ExpAM of which oxide layer was thinner and more uniform.

Figure 6 shows the compositional space the 14 alloys occupy in terms of Al and Cr contents. Superimposed on this plot is encircled groups of alloys that formed the same oxide scales during testing—as observed in Figure 4. Alloys 1-3 formed Cr_2O_3 while IN713 and ExpAM did not despite the latter having greater Cr content. This illustrates empirically that approximately >10 at. pct Al is required in for Al_2O_3 to be stable and prevent Cr_2O_3 formation given Cr_2O_3 levels of 8–14 at. pct. The alloys that formed both alumina and chromia layers all had AlN present in their subscale microstructure. The precipitation of AlN by the Alloys 1 to 3 and Alloy 1 + Hf was due to N permeation into the material. When it is observed after 24 hours, these 4 alloys all exhibited relatively continuous Al_2O_3 layers, suggesting that the N uptake of the material occurred early on before the Al_2O_3 layers was established. In light of this,

it is concluded empirically that Al content in excess of approximately 11.5 at. pct is required in order for rapid formation of Al_2O_3 to take place and to avoid the formation of aluminum nitrides.

The inclusion of either Ti or Al to achieve increased γ' content has implications for oxidation resistance. In alloys that form γ' with greater Ti content such as ABD900AM, IN738LC, and IN939, the formation of TiN, TiO_2, and Cr_2TiO_5 took place. In high Al content alloys such as Alloys 1 to 3, the phases that formed were Al_2O_3 and AlN. The oxidation kinetics and mass gain of the alumina formers were markedly reduced, hence from an oxidation perspective, achieving a desired γ' volume fraction by increasing Al is more favorable than by increasing the Ti content. The 5 compositions with Ti content greater than 2.7at. pct all formed Ti-rich oxides and TiN, giving an empirical indication of a threshold below which Ti-rich phase precipitation is avoided.

Despite the samples of this study having been processed by AM, the trends highlighted here in terms of influence of Al content are congruous with those reported in the conventionally manufactured alloys.[30] This suggests the influence of composition is of similar if not greater significance when compared with the impact of changing processing method.

D. Implications for design of oxidation resistant superalloys for additive manufacturing

General guidelines for designing AM superalloys for oxidation resistance stem from this work. At first, the extent of Ti content is considered. The findings of this study suggest that Ti content less than 2.7at. pct is desirable in order to limit the formation of Ti-rich oxides. The literature highlights that while increasing the Ti content can increase the activity of Cr, it increases the chromia scale growth rate by injecting vacancies[31,32] and can diffuse through the chromia scale along grain boundaries.[33] Al, Nb, and Ta contents can be increased in order to achieve the desired levels of γ' without the inclusion of deleterious amounts of Ti. The contribution of Nb content must additionally be balanced in order to properly address the mechanical properties of the alloy since Nb and Ta increase the anti-phase boundary energy (APB) of γ' and the ensuing flow stress of the alloy in the precipitate shear deformation regime. It has been shown previously that the balance of Nb and Ta to Al content at a constant γ' volume fraction dictates the alloy performance towards either greater flow stress or oxidation resistance.[5]

The results of this study mapped in Figure 6 illustrate how the Al and Cr contents—and their effective activities[30]—are the primary compositional variables that determine the oxidation resistance of the superalloys. This experimentally generated map shows three principle regimes, one where chromia is the sole continuous passivating oxide layer—populated by alloys such as IN718, IN738LC, and ABD900AM, second, a regime where alumina formed with no chromia (IN713, ExpAM, CM247LC) and lastly a compositional space where both were present (Alloys 1-3). From this, the conclusion can be drawn that Al content greater than
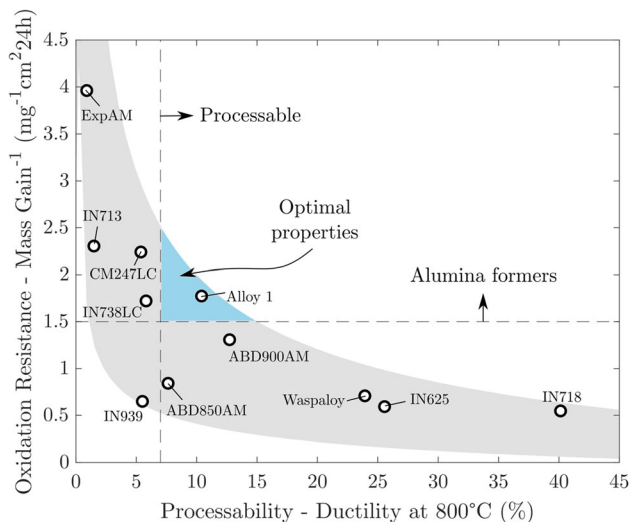
Fig. 7—Plot of oxidation resistance *vs* additive manufacturability illustrating the trade-off between these properties.

7-9 at. pct is required for continuous alumina scale formation, this is key since chromia degrades at elevated air velocities and temperatures of 1000 °C and above.[30] However, it is shown that a compositional space exists promoting the formation of both chromia and alumina scales at 1000 °C. It is noted that the alloys in this compositional space formed aluminum nitrides, likely due to the early-stage uptake of N.

The additive manufacturability/processability of Ni-based superalloys has been shown to depend upon the severity of the ductility loss in the ductility dip regime.[17] Figure 7 illustrates a trade-off between manufacturability and oxidation resistance through comparison of the inverse of mass gain after 24 hours *vs* the 800 °C ductility of these alloys measured in Reference 17. This trade-off results from the influence of Al, which decreases processability by increasing the solution strengthening but greatly improves the oxidation resistance. An optimal alloy property space is shown to exist along the pareto front which must be targeted to ensure both oxidation resistance and the necessary ductility to be processed successfully. While the ductility of a given composition is not the sole factor dictating processability, we emphasize here that at a given level of ductility a range of oxidation resistance performance can be achieved, this is exemplified when contrasting IN939 and CM247LC in Figure 7. This body of work gives insights into the optimal levels of Al, Nb, Ti, Cr, and the optimal property spaces to form desired oxide scales and favorable oxidation kinetics.

IV. SUMMARY AND CONCLUSIONS

1. Thermo-gravimetric testing was performed at 1000 °C on a set of 14 different Ni-based superalloys in an effort to build a consistent dataset describing the early-stage oxidation of alloys produced with the same processing conditions. Correlation between their composition, mass gained during testing, depletion zone size, and oxide layer thickness formed was found. This was coupled with phase identification to develop a compositional map useful for alloy design tailored towards additive manufacturability and oxidation resistance.

2. The compositions with Al content greater than ~9 at. pct were found to rapidly form Al_2O_3 at 1000 °C. A threshold for stable Al_2O_3 formation was identified between 7 and 9 at. pct Al. Design of alloys for additive manufacturing with oxidation resistance at 1000 °C should consider this threshold to avoid the breakdown down of chromia. Furthermore, 11.5 at. pct Al is empirically concluded to be the threshold to form a stable Al_2O_3 scale fast enough to avoid the early uptake of nitrogen and ensuing formation of AlN subscale.

3. Alloys with Ti content of 2.7 at. pct and greater formed Ti-rich oxide phases in their oxide scales as well as TiN subscale. Design of alloys for AM and oxidation resistance with Ti content below this threshold is likely beneficial given the detrimental role of Ti oxides highlighted in the literature.

4. A trade-off between alloy processability and oxidation resistance is identified, dictated by the deleterious effect of Al content on the ductlity dip and the benefit of Al for oxidation resistance. A property space along the pareto front is highlighted, which we noted, represents the ideal design space in which oxidation resistance and processability are both maximized.

CONFLICT OF INTEREST

Alloyed Ltd (formerly OxMet Technologies) is a spin-out company of the University of Oxford, and some of the authors of this manuscript work for this organization, as listed in the affiliations given on the first page of the paper. Prof Reed maintains a small (< 5 pct) shareholding in this company.

REFERENCES

1. D. Herzog, V. Seyda, E. Wycisk, and C. Emmelmann: *Acta Mater.*, 2016, vol. 117, pp. 371–92.
2. S.P. Murray, K.M. Pusch, A.T. Polonsky, C.J. Torbet, G.G. Seward, N. Zhou, S.A. Forsik, P. Nandwana, M.M. Kirka, R.R. Dehoff, et al.: *Nat. Commun.*, 2020, vol. 11(1), pp. 1–1.
3. J. Xu, H. Gruber, R. L. Peng, and J. Moverare: *Materials* (2020), vol. 13 (21), pp. 4930.
4. J.-U. Park, S.-Y. Jun, B.H. Lee, J.H. Jang, B.-S. Lee, H.-J. Lee, J.-H. Lee, and H.-U. Hong: *Addit. Manuf.*, 2022, vol. 52, p. 102680.
5. J.N. Ghoussoub, P. Klupś, W.J. Dick-Cleland, K.E. Rankin, S. Utada, P.A. Bagot, D.G. McCartney, Y.T. Tang, and R.C. Reed: *Addit. Manuf.*, 2022, vol. 52, p. 102608.
6. S.A. Németh, D. Crudden, D. Armstrong, D. Collins, K. Li, A. Wilkinson, C. Grovenor, and R. Reed: *Acta Mater.*, 2017, vol. 126, pp. 361–71.
7. C. Fang, H. Basoalto, M. Anderson, H. Li, S. Williams, and P. Bowen: *J. Mater. Sci. Technol.*, 2022, vol. 104, pp. 224–35.
8. S.A. Cervellon, J. Yi, F. Corpace, Z. Hervier, J. Rigney, P. Wright, C. Torbet, J. Cormier, J. Jones, and T. Pollock: *Superalloys*, 2020, vol. 2020, pp. 185–95.
9. S.A. Sato, Y.-L. Chiu, and R. Reed: *Acta Mater.*, 2011, vol. 59(1), pp. 225–40.
10. S.-J. Park, S.-M. Seo, Y.-S. Yoo, H.-W. Jeong, and H. Jang: *Corros. Sci.*, 2015, vol. 90, pp. 305–12.
11. Y. Koizumi, K. Kawagishi, T. Yokokawa, M. Yuyama, Y. Takata, and H. Harada: *Superalloys*, 2020, vol. 2020, pp. 747–52.
12. S. Yu, X. Zhan, F. Liu, Y. Guo, Q. Wang, Y. Li, Z. Wang, Z. Wang, L. Tan, X. Fan, et al.: *J. Alloys Compd.*, 2022, vol. 904, p. 164071.
13. J. Pistor, S. Hagen, S. Virtanen, and C. Körner: *Scripta Mater.*, 2022, vol. 207, p. 114301.
14. C. Juillet, A. Oudriss, J. Balmain, X. Feaugas, and F. Pedraza: *Corros. Sci.*, 2018, vol. 142, pp. 266–76.
15. T. Sanviemvongsak, D. Monceau, M. Madelain, C. Desgranges, J. Smialek, and B. Macquaire: *Corros. Sci.*, 2021, vol. 192, p. 109804.
16. Y.T. Tang, C. Panwisawas, J.N. Ghoussoub, Y. Gong, J.W. Clark, A.A. Németh, D.G. McCartney, and R.C. Reed: *Acta Mater.*, 2021, vol. 202, pp. 417–36.
17. J.N. Ghoussoub, Y.T. Tang, W.J. Dick-Cleland, A.A. Németh, Y. Gong, D.G. McCartney, A.C. Cocks, and R.C. Reed: *Metall. Mater. Trans A*, 2022, vol. 53A(3), pp. 962–83.
18. C. Wagner: *Z. Phys. Chem.*, 1933, vol. 21(1), pp. 25–41.
19. B. Gleeson: *Mater. Sci. Technol.*, 2000, vol. 1, pp. 173–228.
20. U. Krupp and H.-J. Christ: *Metall. Mater. Trans A*, 2000, vol. 31A(1), pp. 47–56.
21. S. Han and D. Young: *Oxid. Met.*, 2001, vol. 55(3), pp. 223–42.
22. S.A. Vesel, A. Drenik, K. Elersic, M. Mozetic, J. Kovac, T. Gyergyek, J. Stockel, J. Varju, R. Panek, and M. Balat-Pichelin: *Appl. Surf. Sci.*, 2014, vol. 305, pp. 674–82.
23. L. Kumar, R. Venkataramani, M. Sundararaman, P. Mukhopadhyay, and S. Garg: *Oxid. Met.*, 1996, vol. 45(1), pp. 221–44.
24. J. Chen, P. Rogers, and J. Little: *Oxid. Met.*, 1997, vol. 47(5), pp. 381–410.
25. J. Litz, A. Rahmel, M. Schorr, and J. Weiss: *Oxid. Met.*, 1989, vol. 32(3), pp. 167–84.
26. D. Das, V. Singh, and S.V. Joshi: *Mater. Sci. Technol.*, 2003, vol. 19(6), pp. 695–708.
27. T.-K. Tsao, A.-C. Yeh, C.-M. Kuo, and H. Murakami: *Entropy*, 2016, vol. 18(2), p. 62.
28. M. Yoshihara and Y.-W. Kim: *Intermetallics*, 2005, vol. 13(9), pp. 952–58.
29. S.A. Vicente, J. Moreno, J. Tenório, A. Junior, T. Santos, and D. Espinosa: *Oxid. Commun.*, 2018, vol. 41, pp. 195–204.
30. F. Pettit, G. Meier, M. Gell, C. Kartovich, R. Bricknel, W. Kent, and J. Radovich: *Superalloys*, 1984, vol. 85(1), pp. 651–87.
31. M. Abbasi, D.-I. Kim, J.-H. Shim, and W.-S. Jung: *J. Alloys Compd*, 2016, vol. 658, pp. 210–21.
32. H. Mallikarjuna, W. Caley, and N. Richards: *J. Mater. Eng. Perform.*, 2017, vol. 26(10), pp. 4838–46.
33. M. Lapington, D. Crudden, R. Reed, M. Moody, and P. Bagot: *Acta Mater.*, 2021, vol. 206, p. 116626.